International Journal of Heat and Fluid Flow 78 (2019) 108421

Contents lists available at ScienceDirect

International Journal of Heat and Fluid Flow

journal homepage: www.elsevier.com/locate/ijhff

Low-frequency oscillations in flow past an inclined prolate spheroid

Håkon Strandenes[a], Fengjian Jiang[a,*], Bjørnar Pettersen[a], Helge I. Andersson[b]

[a] Department of Marine Technology, Norwegian University of Science and Technology, NO-7491 Trondheim, Norway
[b] Department of Energy and Process Engineering, Norwegian University of Science and Technology, NO-7491 Trondheim, Norway

ABSTRACT

We analyse the forces on a 45° inclined 6:1 prolate spheroid at Reynolds number $Re_D = 8000$. In contrast to flow at lower Reynolds numbers previously investigated, we now find a strong oscillatory behaviour in the global forces. The Strouhal number associated with the forces is 0.05 and the peak-to-peak value of the oscillations in the sideforce is more than 25% of the average. A Fourier transformation of the entire flow field reveals that the cause of the force fluctuations is spatial oscillations in one of the two primary vortices generated behind the spheroid. This phenomena is attributed to a three-dimensional vortex instability.

1. Introduction

The flow past a 45° inclined 6:1 (length:diameter) prolate spheroid has been subject to several numerical studies recently with emphasis on investigating details in the wake flow for cases up to $Re_D = 3000$ (Jiang et al., 2014; 2015a; 2015b; 2016). The main motivation for studying this case is the flow features common for many vehicles in the air and ocean space. Based on the results from both simulations and experiments, there is acceptance for the resulting wake flow and forces on the spheroid to be asymmetric, despite the symmetric geometry and inflow condition. This applies to many inclined slender body flow cases (Moskowitz et al., 1989; Cobleigh, 1994; Ashok et al., 2015).

Being a prototype for various vehicles, such as airplanes, drones, ROVs and submarines, focus in this work is on the manoeuvring capabilities and the external forces acting on the spheroid. We have learned from previous studies that the time-averaged wake exerts a significant mean side force on the spheroid, which can be up to 75% of the mean drag force in the range $Re_D = 3000$ to 4000 (see e.g. Jiang et al., 2015b and Strandenes et al., 2019). Considering the engineering background of the inclined spheroid, it is interesting to investigate how strong this side force becomes and how it vary when the Reynolds number is further increased. This is the primary scope of the present study. At Reynolds number $Re_D = 3000$, very low-frequency oscillations of the side force were detected, see e.g. Fig. 2 in (Jiang et al., 2015b), but were not carefully studied. In this $Re_D = 3000$ case there were not observed any similar oscillations in the drag and lift forces. It is assumed that three-dimensional effects could be the mechanism behind it, as addressed by Jiang et al. (2015b) and Zeiger et al. (2004). Some recent works on the wake behind sharp-nosed slender bodies at high incidence indicate similar low frequency forces from vortex oscillations other than vortex shedding (see e.g. Ma and Liu, 2014 and Ma and Yin, 2018). However, in more recent DNS simulations of the actual 6:1 inclined prolate spheroid at $Re_D = 4000$ (Strandenes et al., 2019), the regular low-frequency oscillations observed at $Re_D = 3000$ are no longer present, and only high-frequency irregular oscillations remain. It is therefore of great interest to investigate how the forces on the spheroid develop as the Reynolds number is increased. In the present paper, we will address these points by discussing results obtained by Direct Numerical Simulation (DNS) at $Re_D = 8000$.

Fig. 1 shows the computational domain along with its dimensions. The flow is governed by the mass conservation and Navier–Stokes equations for incompressible flow. The constant inflow velocity is uniform with $u = U_\infty$, $v = w = 0$. The outlet is a fixed-pressure boundary condition with zero-gradient Neumann conditions for the velocity. The four other side boundaries of the domain, perpendicular to the y and z-axes, are slip-walls in which the wall-normal velocity component is prescribed to be zero, while the other velocity components and the pressure have a zero-gradient Neumann condition. The Reynolds number based on the equatorial diameter D is $Re_D = DU_\infty/\nu = 8000$.

2. Numerical methods

The code *MGLET* (Manhart et al., 2001) is used for the simulations presented in this paper. In short, MGLET uses a finite-volume formulation on staggered Cartesian grids to solve the incompressible Navier–Stokes equations. Linear interpolation and integration for all spatial terms are used, leading to second-order accuracy in space. A third-order low-storage explicit Runge–Kutta time integration scheme (Williamson, 1980) is used for time stepping. The solid geometry is introduced through an immersed boundary method (Peller et al., 2006). A combined multi-grid and local grid refinement method is used to, *i)*

* Corresponding author.
E-mail address: fengjian.jiang@ntnu.no (F. Jiang).

https://doi.org/10.1016/j.ijheatfluidflow.2019.05.010
Received 11 September 2018; Received in revised form 13 May 2019; Accepted 13 May 2019

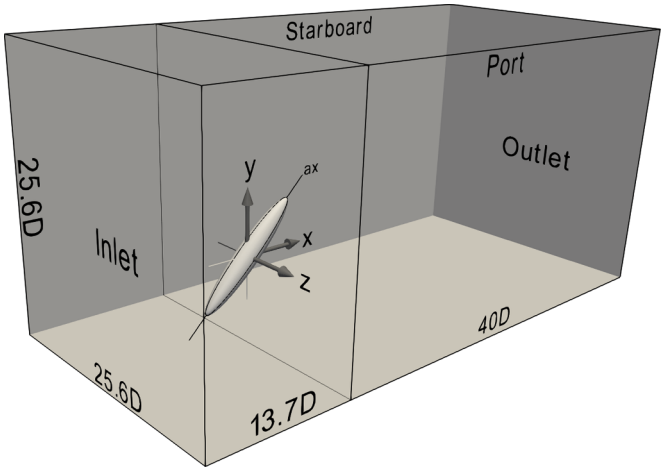

Fig. 1. Computational domain and coordinate system. The origin of the coordinate system is in the center of the spheroid. The figure is not to scale.

increase the convergence rate of the pressure solver and, *ii)* resolve geometrical and flow structures sufficiently (Manhart, 2004). The grid is entirely isotropic, i.e. $\Delta x = \Delta y = \Delta z$ everywhere in the domain.

To justify that the grid resolution is sufficient for the problem in question, we performed a grid resolution study. Three different meshes with different resolution were created (see Table 1), and a fully developed flow field was computed on the finest grid. This solution was then transferred to the two coarser grids, and the three simulations were restarted and run for the same number of timesteps.

Fig. 2 gives an overview of the results. The coarsest grid tested in this convergence study is clearly not satisfactory. The initial condition is a flow field with a strongly asymmetric side force C_{Fz}, which quickly develops into a nearly symmetric flow state with almost zero mean sideforce after restarting with the coarser grid. On the two finer grids (medium and fine), the asymmetric side force persists, but there are still differences in the computed forces. The power spectra of the v-velocity in a selected point in the wake, as shown to the left in Fig. 2, also indicate that the flow on the coarsest grid is severely under-resolved. A major portion of the energy at the higher frequencies is lost. The two finest grids show reasonable agreement, but the finer grid clearly resolve more scales compared to the medium grid. In conclusion, we believe that the finest grid is sufficiently fine to resolve all essential scales present in this flow with the required precision. Measured in a plane at $x/D = 4$, the grid resolution Δx is never larger than about 1.4 times the estimated Kolmogorov lengthscale η, i.e. $\max(\Delta x/\eta) = 1.4$. The results discussed hereafter are all from the simulation using the finest mesh.

3. Results

In general, the flow structures in this flow configuration at $Re_D = 8000$ share many similarities with the flow at lower Reynolds numbers ($Re_D = 3000$), as referred to in the introduction. However, there are a few important distinctions. Fig. 3 gives an overview of the flow structures of the present case, and shows the two main coherent vortices originating from the tip, here named S and P. The weaker of the two vortices is P and the stronger one is S, by means of maximum vorticity in the vortex core. The figure clearly shows that the weaker one, P, is the one to disintegrate closest to the nose. This is the opposite of the lower Reynolds number cases, where the weakest of the two vortices was the most stable structure, persisting far downstream of the spheroid tail. Further details and analysis of the wake will be subject to a separate study and will not be presented herein.

We present the mean and RMS of the force coefficients compared to earlier results in Table 2. From this we observe that the mean drag coefficient C_{Fx} decreases as the Reynolds number increases, while in the two other directions the coefficients C_{Fy} and C_{Fz} increase. This means that the side forces become more significant at $Re_D = 8000$ compared to for instance $Re_D = 3000$. Furthermore, there is one phenomenon that has never been reported before, that is a very strong low-frequency oscillation in the forces from the fluid acting on the spheroid in all three directions. Fig. 4 gives an overview of the evolution of the force coefficients, from which this phenomenon is evident. In contrast to the oscillations in the sideforce observed at $Re_D = 3000$ these oscillations are now working in all directions: lift (F_x), drag (F_y) and sideways (F_z). This paper aims to present a concise and focused study on this phenomenon.

The period of these low-frequency oscillations are almost exactly $T = 1/f = 20\ D/U_\infty$, leading to a Strouhal number of $St = fD/U_\infty = 0.05$. Compared to a typical vortex street behind a circular cylinder at similar Reynolds number with Strouhal number of $St = 0.2$, the present oscillation is surprisingly slow. One easily notice from Fig. 4, that the peak-to-peak side force C_{Fz} oscillations is more than 25% of their mean value, revealing very strong flow dynamics in the wake that heavily influences the near pressure field. However, by inspections of the velocity field in the wake, we cannot find any signs of vortex shedding, and the presence of a von Karman vortex street can be ruled out. By using visualization in 2-D and 3-D of quantities such as velocity, pressure, vorticity, λ_2 etc., no obvious other structures can be attributed to this phenomenon either.

In order to identify the source of these low-frequency oscillations, we employ a simple, novel technique we call *in-situ Fourier transform*. In this technique we evaluate a discrete Fourier transform of the entire pressure field for selected, pre-defined frequencies. This evaluation is performed in discrete time windows. Once each window is finished, the results are added to an accumulated, time-averaged Fourier coefficient for the selected frequencies. The real part of this Fourier coefficient is the total energy content of the selected wavelength, and is computed for every gridcell in the computational domain. In practice, the results are the same as if we had stored the pressure in every gridcell every timestep, and computed the energy spectra from these data, but only extracted the energies corresponding to a few frequencies. Therefore, this technique is especially economical and effective for DNS in light of the enormous number of grid cells used in the simulations.

The result is shown in Fig. 5. The red areas indicate zones where the pressure fluctuates strongly with $f = 1/20\ U_\infty/D$, and the blue areas indicate zones where the pressure fluctuates with frequency $2f = 2/20\ U_\infty/D$. The observed pattern can easily be explained: there is a cyclic motion of the two main wake vortices. The strongest vortex (S), which is located to the left in Fig. 5, moves from the leftmost red area (where it is strong), passing through the blue area (where it gets weaker or the path is more uncertain), and towards the next red area again, before it returns back the same path towards the origin at the leftmost red area. The vortex passes through the blue area twice per cycle, hence the double frequency. The pattern of this motion is an upside-down 'U'-pattern.

The weaker main vortex (P) also exhibits a similar motion, but along an almost vertical line instead of the curved path of the stronger vortex. In addition, the vortex itself is much weaker, and thus the energies recorded are lower.

To further understand the motion of this vortex and how it influences the forces on the spheroid, additional simulations were carried out. In these simulations, the pressure was recorded in several planes perpendicular to the x-axis. From these time series, we identified the location of the vortex core by searching for the position of the lowest pressure. The trajectories of the vortex center in each x-plane, are shown in Fig. 6. Each dot corresponds to the position of the vortex core at a time instant, and the color indicates the strength of the vortex core at that time.

From Fig. 6 we can see that the motion of the vortex core at $x/D = 0.0$ is already visible, and forms an elliptical path. By the colouring, we also observe that the vortex core vary in strength throughout

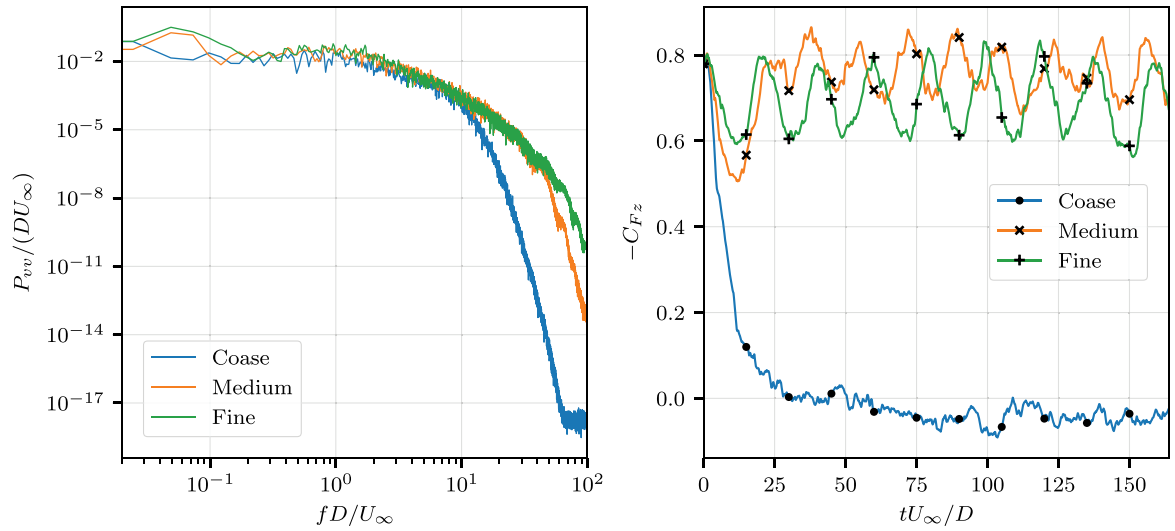

Fig. 2. Results from the grid resolution study. Left: Power spectra of v-velocity sampled in point $(x, y, z) = (2.5, 1.32, 0.5)D$. Right: Sideforce coefficient C_{Fz} as a function of time.

Table 1
Grid convergence study setup. All cases were simulated 163,840 timesteps starting from the same initial condition, and the timestep was 0.001 D/U_∞ in all cases. Δx is the grid resolution and η is an estimate of the Kolmogorov length scale.

Simulation	Coarse	Medium	Fine
Number of grid cells	0.447×10^9	1.660×10^9	2.077×10^9
$\min(\Delta x/D)$	0.016	0.008	0.004
$\max(\Delta x/\eta)$ at $x/D = 4.0$	5.11	2.69	1.38

this oscillatory motion. When the vortex core is furthest away from the spheroid, it is usually stronger than when the vortex core is closer to the body. In the plane $x/D = 0.5$ the circular path has transformed into a line. At $x/D = 1.0$ the elliptical shape is yet again visible. Also here, it is evident that the vortex core is stronger when it is in a position further away from the body than when it is close. Finally, at we see the same 'U'-shape as we predicted based on the in-situ Fourier transform. We also see, that the vortex core oscillates both in strength and position. This explains why the two red areas to the left in Fig. 5 are of different magnitude.

The trajectories of the vortex cores are plotted along with the pressure in an attached animation, from which we unexpectedly notice that the motion of the vortex core is anti-clockwise at $x/D = 0.0$ but clockwise at $x/D = 1.0$. In the plane $x/D = 0.5$ the motion is back and forth a straight path. This interesting observation is also marked with arrows in Fig. 6. The plots in Fig. 6 show that the vortex tube is under both a wave type motion in the axial direction and a helical motion, therefore suggesting the three-dimensional vortex instability (Ash and Khorrami, 1995). The frequency of this instability coincides with the frequency of the overall body forces.

It is furthermore interesting to notice, from Fig. 6, that the spatial oscillation of the vortex is accompanied by pressure (C_p) variation, meaning the source of the oscillatory body forces may come from either the spatial oscillation or the pressure variation, or the joint effect of them. To clarify this, we plot the correlation between the side force (C_{Fz}) and the vortex core location in plane $x/D = 0.0$ in Fig. 7. The abscissa is the distance, ℓ, from the center of the spheroid

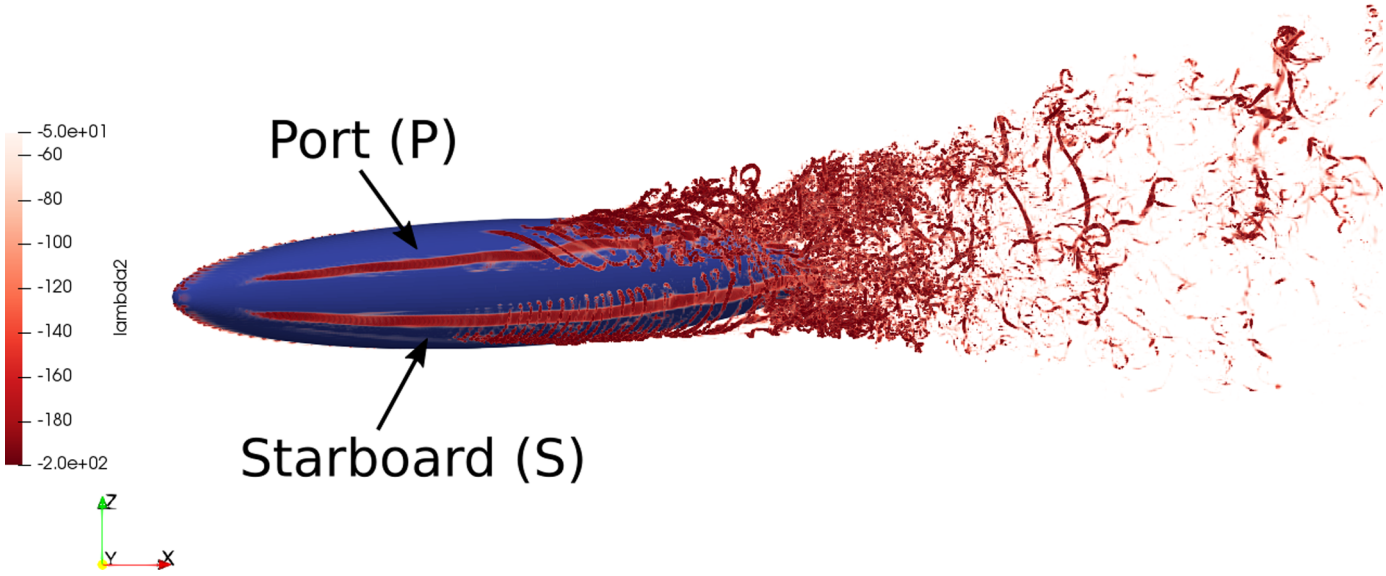

Fig. 3. Looking from below on the wake visualized by a volume rendering of the λ_2 vortex identification criterion. The strongest of the two vortices is the starboard vortex.

Table 2
Mean and root-mean-square (RMS) of the force and torque coefficients.

Re_D		C_{Fx}	C_{Fy}	C_{Fz}	C_{Mx}	C_{My}	C_{Mz}
3000 (ref. Jiang et al., 2015b)	Mean	0.879	−0.796	−0.645	−0.168	0.166	0.311
	RMS				0.009	0.009	0.010
4000 (ref. Strandenes et al., 2019)	Mean	0.852	−0.807	0.637	0.084	−0.082	0.315
	RMS	0.012	0.013	0.039	0.019	0.019	0.015
8000 (present)	Mean	0.832	−0.831	−0.701	−0.123	0.122	0.316
	RMS	0.022	0.014	0.069	0.023	0.023	0.014

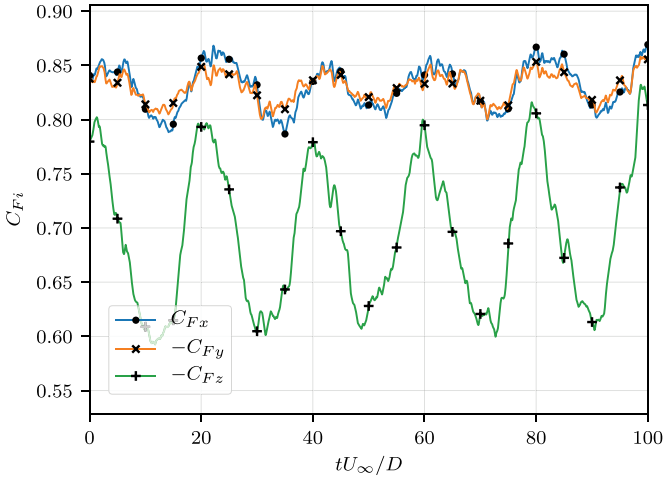

Fig. 4. Drag and sideways force coefficients at $Re_D = 8000$ for the first 100 D/U_∞ simulated.

$((x, y, z) = (0, 0, 0))$ to the vortex core position in the plane $x = 0$. We clearly observe that the side force is stronger as the vortex moves closer to the spheroid, however, the colours in Fig. 7 indicated that the pressure is higher as the vortex is closer to the spheroid, which seems to be contradictory. Further investigation of C_p and the side force shows no correlation between them. Additionally, we do not find any correlations between C_p in the vortex core at $x/D = 0.0$ and $x/D = 1.0$, at the same instant. This tells us that the variation in pressure in the vortex core is a local phenomenon and does not influence the overall integrated force on the spheroid. Therefore, the oscillatory body force is only caused by the spatial oscillation of the vortex, which is originally induced by the three-dimensional vortex instability.

4. Concluding remarks

The low-frequency forces acting on the 6:1 prolate spheroid at Reynolds number $Re_D = 8000$ is of great importance for manoeuvring capabilities of vehicles. The period of the observed low-frequency phenomenon is four times that of typical vortex shedding from cylinders. This unexpected phenomenon is caused by the cyclic motion of the primary wake vortex, which oscillates both in strength and space. The spatial oscillations seem to be the dominant source of the oscillatory

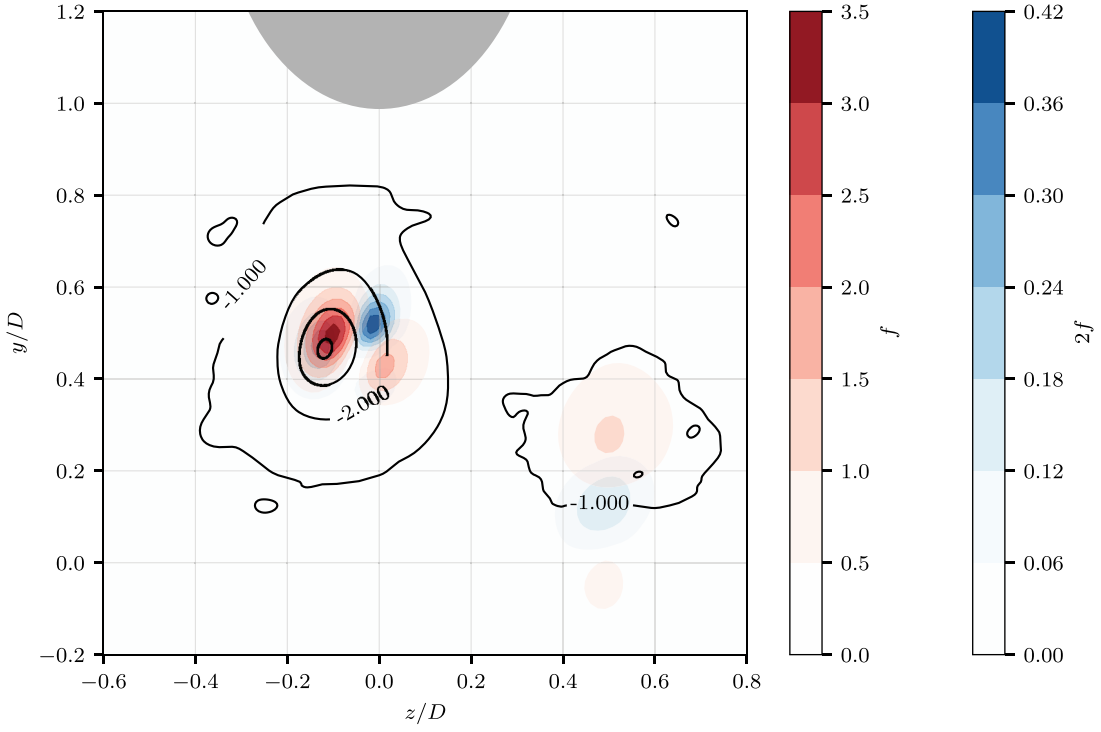

Fig. 5. yz-plane at $x/D = 1.55$. Spheroid cross-section is grey. Fourier amplitudes of the pressure at the frequency corresponding to the low-frequency oscillations in the forces $f = 1/20\ U_\infty/D$ (red colors) and the double of this frequency $2f = 2/20\ U_\infty/D$ (blue colors). The pressure coefficient $C_p = p/(0.5\rho U_\infty^2)$ from a randomly selected timestep is drawn with black iso-contours. (For interpretation of the references to colour in this figure legend, the reader is referred to the web version of this article.)

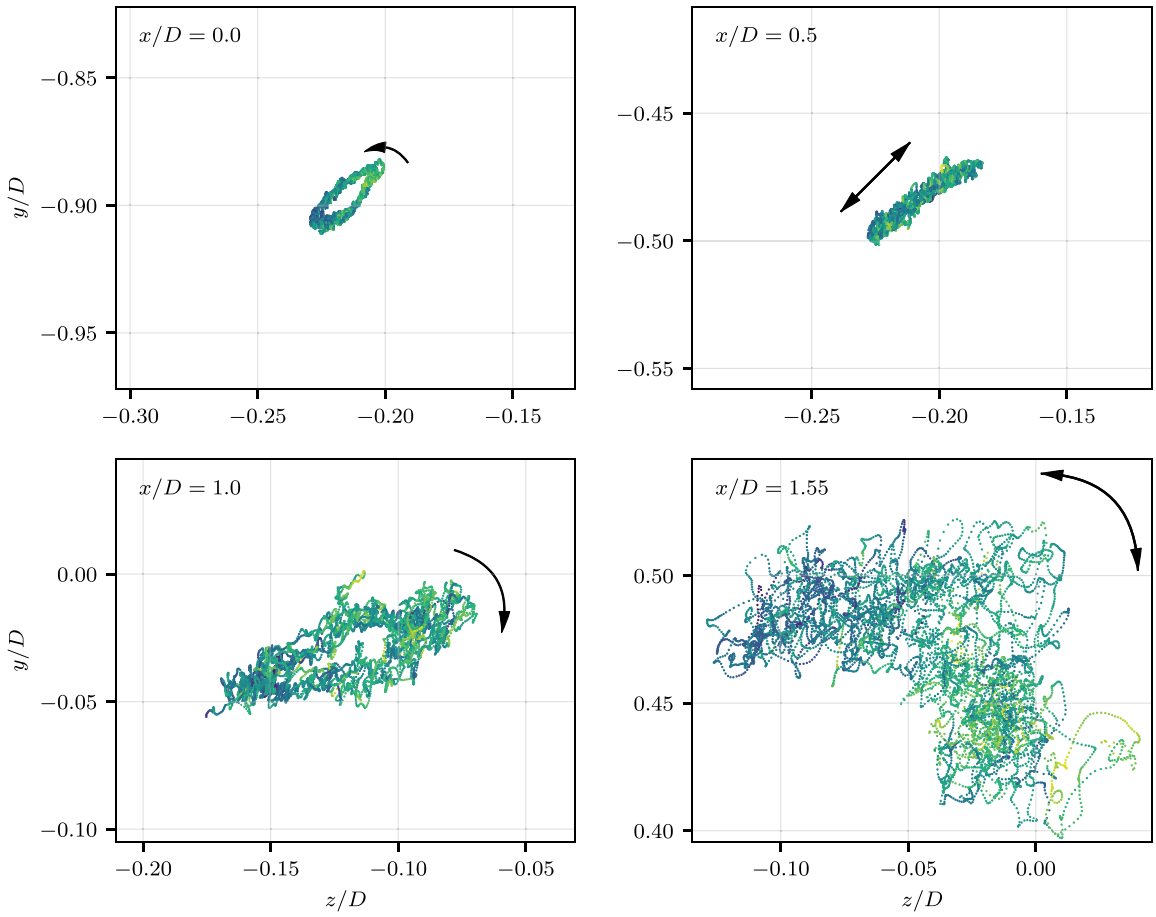

Fig. 6. The trajectories of the vortex core in four yz-planes at different x-locations. Each point corresponds to the position of the vortex core at one time instance. The colours of the point correspond to the pressure of the vortex core. Darker colours (deep blue) indicate lower pressure and stronger suction while lighter colours (yellow) indicate higher pressure and weaker suction. A total of five cycles ($100\, D/U_\infty$) are plotted. In all plots, the spheroid is located above and to the right. Arrows indicate direction of path. (For interpretation of the references to colour in this figure legend, the reader is referred to the web version of this article.)

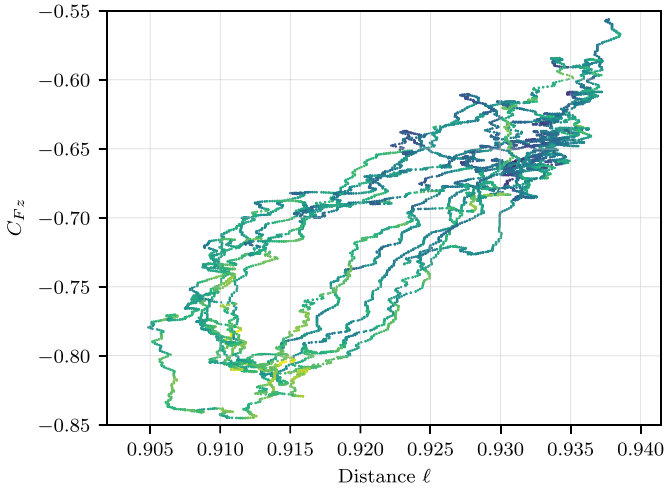

Fig. 7. Correlation between the overall sideforce on the spheroid body and the distance l from the vortex core to the point $(y, z) = (0, 0)$ in the plane $x/D = 0.0$. The colours indicate C_p as described in the caption of Fig. 6.

forces, because the variations in strength are in local regions only. The exploration of this phenomenon is still on-going. Simulations at higher Reynolds numbers are in progress, and seem to confirm that the oscillations are still present at higher Re_D.

The phenomenon is similar to the phenomena reported by Ma and Liu (2014) and Ma and Yin (2018), however, the absence of vortex shedding in the present configuration makes the flow and wake configuration qualitatively different from their results.

Acknowledgments

Computing time was granted by UNINETT Sigma2 under project *nn9191k*. F.J. acknowledges the funding from the Future Industry's Leading Technology Development program (No. 10042430) of MOTIE/KEIT of Korea.

Supplementary materials

Supplementary material associated with this article can be found, in the online version, at doi:10.1016/j.ijheatfluidflow.2019.05.010.

References

Ash, R.L., Khorrami, M.R., 1995. Vortex stability. In: Green, S.I. (Ed.), Fluid Vortices. Springer Science + Business Media B.V., pp. 317–372. https://doi.org/10.1007/978-94-011-0249-0_8.

Ashok, A., Van Buren, T., Smits, A., 2015. Asymmetries in the wake of a submarine model in pitch. J. Fluid Mech. 774, 416–442. https://doi.org/10.1017/jfm.2015.277.

Cobleigh, B., 1994. High-angle-of-attack yawing moment asymmetry of the X-31 aircraft from flight test. 12th Applied Aerodynamics Conference. pp. 1803. https://doi.org/10.2514/6.1994-1803.

Jiang, F., Andersson, H.I., Gallardo, J.P., Okulov, V.L., 2016. On the peculiar structure of a helical wake vortex behind an inclined prolate spheroid. J. Fluid Mech. 801, 1–12. https://doi.org/10.1017/jfm.2016.428.

Jiang, F., Gallardo, J.P., Andersson, H.I., 2014. The laminar wake behind a 6:1 prolate spheroid at 45° incidence angle. Phys. Fluids 26 (11), 113602. https://doi.org/10.1063/1.4902015.

Jiang, F., Gallardo, J.P., Andersson, H.I., 2015a. Transition and loss of symmetry in the wake behind an inclined prolate spheroid. In: Skallerud, B., Andersson, H.I. (Eds.), 8th National Conference on Computational Mechanics MekIT'15. International Center for Numerical Methods in Engineering (CIMNE), Barcelona, Spain, pp. 219–232.

Jiang, F., Gallardo, J.P., Andersson, H.I., Zhang, Z., 2015b. The transitional wake behind an inclined prolate spheroid. Phys. Fluids 27 (9), 093602. https://doi.org/10.1063/1.4929764.

Ma, B.-F., Liu, T.-X., 2014. Low-frequency vortex oscillation around slender bodies at high angles-of-attack. Phys. Fluids 26 (9), 091701. https://doi.org/10.1063/1.4895599.

Ma, B.-F., Yin, S.-L., 2018. Vortex oscillations around a hemisphere-cylinder body with a high fineness ratio. AIAA J. 56 (4), 1402–1420. https://doi.org/10.2514/1.J056047.

Manhart, M., 2004. A zonal grid algorithm for DNS of turbulent boundary layers. Comput. Fluids 33 (3), 435–461. https://doi.org/10.1016/s0045-7930(03)00061-6.

Manhart, M., Tremblay, F., Friedrich, R., 2001. MGLET: a parallel code for efficient DNS and LES of complex geometries. In: Jenssen, C.B., Kvamdal, T., Andersson, H.I., Pettersen, B., Ecer, A., Periaux, J., Satofuka, N., Fox, P. (Eds.), Parallel Computational Fluid Dynamics - Trends and Applications. Elsevier Science B.V., pp. 449–456. https://doi.org/10.1016/B978-044450673-3/50123-8.

Moskowitz, C., Dejarnette, F.R., Hall, R.M., 1989. Effects of nose bluntness, roughness, and surface perturbations on the asymmetric flow past slender bodies at large angles of attack. 7th Applied Aerodynamics Conference. pp. 2236. https://doi.org/10.2514/6.1989-2236.

Peller, N., Duc, A.L., Tremblay, F., Manhart, M., 2006. High-order stable interpolations for immersed boundary methods. Int. J. Numer. Methods Fluids 52 (11), 1175–1193. https://doi.org/10.1002/fld.1227.

Strandenes, H., Jiang, F., Pettersen, B., Andersson, H.I., 2019. Near-wake of an inclined 6:1 spheroid at Reynolds number 4000. AIAA J. 57 (4), 1364–1372. https://doi.org/10.2514/1.J057615.

Williamson, J.H., 1980. Low-storage Runge–Kutta schemes. J. Comput. Phys. 35 (1), 48–56. https://doi.org/10.1016/0021-9991(80)90033-9.

Zeiger, M., Telionis, D., Vlachos, P., 2004. Unsteady separated flows over three-dimensional slender bodies. Prog. Aerosp. Sci. 40 (4–5), 291–320. https://doi.org/10.1016/j.paerosci.2004.06.002.